# Theory of the nonreciprocal Josephson effect

Kou Misaki[1,*] and Naoto Nagaosa[1,2]
[1]*Department of Applied Physics, The University of Tokyo, Bunkyo, Tokyo 113-8656, Japan*
[2]*RIKEN Center for Emergent Matter Science (CEMS), Wako, Saitama 351-0198, Japan*

(Received 22 March 2021; revised 29 April 2021; accepted 17 May 2021; published 1 June 2021)

The heterojunction between different materials often exhibits a rectifying effect; e.g., pn junction is used for diode. On the other hand, the Josephson junction between two different superconductors is assumed to show symmetric response between two directions of the current, i.e., the voltage drop $V$ is antisymmetric with respect to the sign change of the current $I$. However, there should be an asymmetry between the states of charge accumulation on the right and left sides of the Josephson junction, which can lead to the nonreciprocal responses. Here we demonstrate theoretically that nonreciprocal $I$-$V$ characteristic appears due to this charging energy difference both in the classical and quantum regimes.

DOI: 10.1103/PhysRevB.103.245302

## I. INTRODUCTION

Nonreciprocal responses in noncentrosymmetric materials in general have been actively studied both from theoretical and experimental viewpoints [1]. It is often the case that broken $\mathcal{T}$, the time-reversal symmetry, is needed in addition to broken $\mathcal{P}$, the inversion symmetry, to obtain the nonreciprocal responses, but there are cases where only $\mathcal{P}$ breaking is enough. The pn junction is a representative example, where the heterojunction of n-type and p-type semiconductors acts as a rectifier without a magnetic field or magnetization. On the other hand, the direction of the arrow of time is determined by the dissipation associated with the resistivity, i.e., irreversibility. In the case of pn junction, the existence of the depletion layer due to the Coulomb interaction is essential for its rectification function. Another example of the nonreciprocal response without $\mathcal{T}$ breaking is the Zener tunneling [2]. In this case, the interband tunneling probability across the band gap differs between right and left directions due to the shift vector originating from the Berry connection [3], even without the broken $\mathcal{T}$. This shift vector is also relevant to the shift current for the interband photoexcitation [4]. Therefore, the quantum geometry, which encodes the information of the microscopic inversion asymmetry inside a unit cell, plays an important role. The nonreciprocity in optical systems has been widely studied [5], and in particular, the quantum diode of light has been theoretically studied [6] and experimentally realized [7]. Here the two isolated two level systems act as nonlinear mirrors and lead to a left-right asymmetric Fabry-Perot interferometer. Also, as for the Josephson junctions, there are studies on the Josephson diode [8–15], but the nonreciprocity of the voltage drop of the single Josephson junction has not been studied.

Other works on the nonreciprocity include Ref. [16], where the nonreciprocal property of the microwave reflection of the resistively shunted Josephson junction in the finite voltage state is investigated. In Ref. [16], the inversion symmetry is explicitly broken by the external current bias, and the nonreciprocity in the AC regime, characterized by the asymmetry of the scattering matrix, is discussed. In contrast, our work focuses on the nonreciprocity of the structurally inversion asymmetric Josephson junction in the DC regime, which is characterized by the $I$-$V$ characteristic as

$$V(I) \neq -V(-I) \Leftrightarrow R(I) \neq R(-I), \tag{1}$$

where $I$ is the DC external current bias, $V$ is the DC voltage response, and $R(I) = V(I)/I$ is the $I$-dependent nonlinear resistance, i.e., the nonreciprocity is quantified by the difference of the nonlinear resistance between positive and negative biases with fixed amplitudes of the biases.

The nonreciprocity of the $I$-$V$ characteristic defined by Eq. (1) in the $I \to 0$ limit can be calculated from the perturbative expansion of $R(I)$ as $R(I) = R_1 + R_2 I + \mathcal{O}(I^2)$, where nonzero $R_2$ indicates the nonreciprocity. This characterization of the nonreciprocity by $R_2$ is inappropriate for the case with large current bias $I$ where the system is in the nonlinear regime so that the perturbative expansion is invalid. For example, in pn junctions, the nonreciprocity is particularly large when the voltage bias is larger than the forward threshold voltage, i.e., in the nonlinear regime. The large nonreciprocity persists up to the critical voltage of the electric breakdown for the backward bias. Therefore, in this case, the difference of the critical voltage for positive and negative biases leads to the nonreciprocal $I$-$V$ characteristic. As for the Josephson junction, it is known [17] that the $I$-$V$ characteristic exhibits the finite critical current between finite and zero voltage state. The difference of this critical current between positive and negative biases in a single Josephson heterojunction has not been studied. In this work, we discuss the difference of the critical current between positive and negative biases, and the resultant nonreciprocity of the structurally asymmetric Josephson junctions.

Before discussing the nonreciprocity, here we review the physics of the Josephson junction to introduce our model. Josephson effect is a representative macroscopic quantum

*mk940se@gmail.com

 

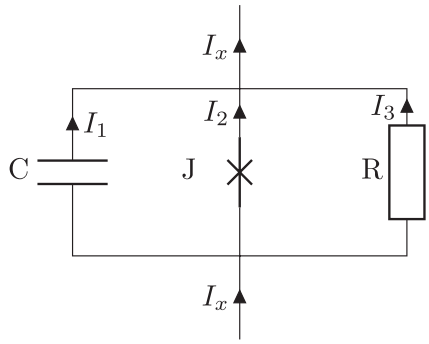


FIG. 1. The Josephson circuit, where $C$, $J$, and $R$ represent the capacitor, Josephson junction, and resistive shunt, respectively. $I_1$, $I_2$, and $I_3$ denote the currents flowing through the capacitive, inductive, and resistive channels of the junction, respectively, and $I_x$ is the total current through the junction.

phenomenon where the superconducting current depends on the phase difference $\varphi$ of the order parameters of the two superconductors separated by the insulating barrier. The dynamics of $\varphi$ in the dissipationless case is characterized by the following Hamiltonian:

$$H = \frac{Q^2}{2C} + E_J\left(1 - \cos\frac{2e\phi}{\hbar}\right) - I_x\phi, \tag{2}$$

where $\phi = \hbar\varphi/(2e)$, $C$ is the capacitance of the Josephson circuit, $Q$ is the charge accumulated at the capacitance, $E_J$ is the Josephson coupling energy, $-e < 0$ is the charge of an electron, $[\phi, Q] = i\hbar$, and $I_x$ is the external current bias, which is assumed to be constant. In this section, for the purpose of illustration, we assume the symmetric charging energy: $Q^2/(2C)$, i.e., $Q$ and $-Q$ are equivalent. We will discuss the consequences of the asymmetric charging energy in the following sections. Equation (2) can be regarded as the Hamiltonian of a particle under the tilted cosine potential with the period $\delta\phi = \pi\hbar/e$, where $Q$ and $\phi$ can be regarded as the momentum and position of the particle, respectively. When $I_x$ is small, near the local minimum of the potential, the potential energy can be approximated by the one of the harmonic oscillator where the mass $m = C$ and the characteristic frequency $\omega = (2e/\hbar)\sqrt{E_J/C}$. Then, the width of the wave function around the potential minima is given by $\Delta\phi = \sqrt{\hbar/(m\omega)}$, and the overlap of the wave functions between the adjacent minima is negligible when $\Delta\phi \ll \delta\phi \Leftrightarrow E_J/E_Q \gg 1$ [case (I)] and large when $\Delta\phi \gg \delta\phi \Leftrightarrow E_J/E_Q \ll 1$ [case (II)], where $E_Q = e^2/(2C)$. We also include the resistive shunt, and the Josephson circuit we will discuss is schematically shown in Fig. 1.

In the case (I), $\varphi$ is well localized inside the minima, and including the resistive shunt, the dynamics is described by the semiclassical Josephson equation given as [18]

$$\hbar\dot{\varphi} = 2eV, \tag{3}$$

$$\dot{Q} + I_c\sin\varphi + \frac{V}{R} = I_x, \tag{4}$$

where $I_c = 2eE_J/\hbar$, $V$ is the chemical potential (voltage) drop across the junction, and $R$ is the shunt resistance. In this paper, we consider the junctions where the tunneling conductance is negligible compared to the shunt conductance. In this case, $R$ is determined by the intrinsic resistance of the normal layer, so that $R$ is symmetric under the voltage inversion and does not contribute to the nonreciprocity. Therefore, we assume that $R$ is constant throughout this paper. We note that $\dot{Q}$ is different from $I_x$, since $\dot{Q}$ is the time evolution of the charge accumulated on the capacitance and different from the total current across the junction $I_x$. Here we neglected the quantum decay probability from the metastable solution where $\varphi$ is localized around the local minima, which is known [19] to be expressed as $P \propto \exp[-AE_J/(\hbar\omega)] = \exp[-A\sqrt{E_J/(8E_Q)}] \ll 1$ at zero temperature in the dissipationless case, where $A$ is the constant factor. We note that the dissipation further suppresses the quantum decay probability [19].

In the absence of the capacitance, i.e., $\dot{Q} = 0$, the $I_x$-$V$ characteristic is solved easily to give $V = 0$ for $|I_x| < I_c = 2eE_J/\hbar$ and the time-averaged voltage $\bar{V} = \mathrm{sign}(I_x)R\sqrt{I_x^2 - I_c^2}$ for $|I_x| > I_c = 2eE_J/\hbar$. Therefore, in this case, the response is reciprocal, as shown in Fig. 2(a), blue curve. In the presence of the capacitance $C$, i.e., $Q = CV$, the differential equation becomes second order, i.e., the inertia term of $\varphi$ appears: It results in the coexistence of the two solutions for a range of $I_x$ and hysteretic behavior of $I_x$-$V$ characteristic, see Fig. 2(b), blue curve. We will numerically show that, in this case, the nonreciprocal $I_x$-$V$ characteristic is realized if we include the effect of the inversion asymmetry coming from the charging energy [see Fig. 2(c)]. To understand why $\dot{Q}$ term in Eq. (4) is necessary for the nonreciprocal effect, here we discuss the inversion symmetry $\mathcal{P}$ and the time reversal symmetry $\mathcal{T}$, of Eqs. (3) and (4), in the absence of $\dot{Q}$ term. $\mathcal{T}$ transforms $I_x \to -I_x$, $\varphi \to -\varphi$, while $V \to V$ as we can see from Eq. (3). Note here that the last term on the left hand side of Eq. (4) changes sign when $\mathcal{T}$ is applied, although $V$ is even with respect to $\mathcal{T}$. This is usual since $1/R$ represents the dissipation and irreversibility, and introduces the asymmetry between the two directions of time. As for the inversion symmetry $\mathcal{P}$, on the other hand, the transformation gives $I_x \to -I_x$, $\varphi \to -\varphi$, and $V \to -V$ since the two bulk superconductors are exchanged. Therefore, the nonreciprocal response, if it exists, comes from the term $\dot{Q}$ in Eq. (4) when the spatial inversion symmetry $\mathcal{P}$ is broken.

In the case (II), since the cosine potential is small, $Q$ is the good quantum number. In the same spirit as the nearly free electron approximation, $E_J(1 - \cos[2e\phi/\hbar])$ term in the Hamiltonian, Eq. (2), can be treated perturbatively, and it leads to the Bragg reflection and opens up a gap at the "momentum" $Q = \pm\hbar\pi/\delta\phi = \pm e$ [20]. The size of the gap is proportional to $E_J$, and the energy at Brillouin zone edge is $E_Q$, so the dimensionless quantity $E_J/E_Q$ is roughly the ratio of the band gap to the bandwidth. The last term in Eq. (2) can be regarded as the potential coming from the external electric field $E = I_x$, and, including the dissipation term, the dynamics of $Q$ is described by the following equation:

$$\dot{Q} = I_x - \frac{1}{R}\frac{\partial\tilde{E}_{ch}(Q)}{\partial Q}, \tag{5}$$

where $\tilde{E}_{ch}(Q)$ is the band energy with the gap at $Q = \pm e$. To discuss the nonreciprocal $I$-$V$ characteristic, we will show that the Bloch oscillation and the Zener tunneling for the dynamics

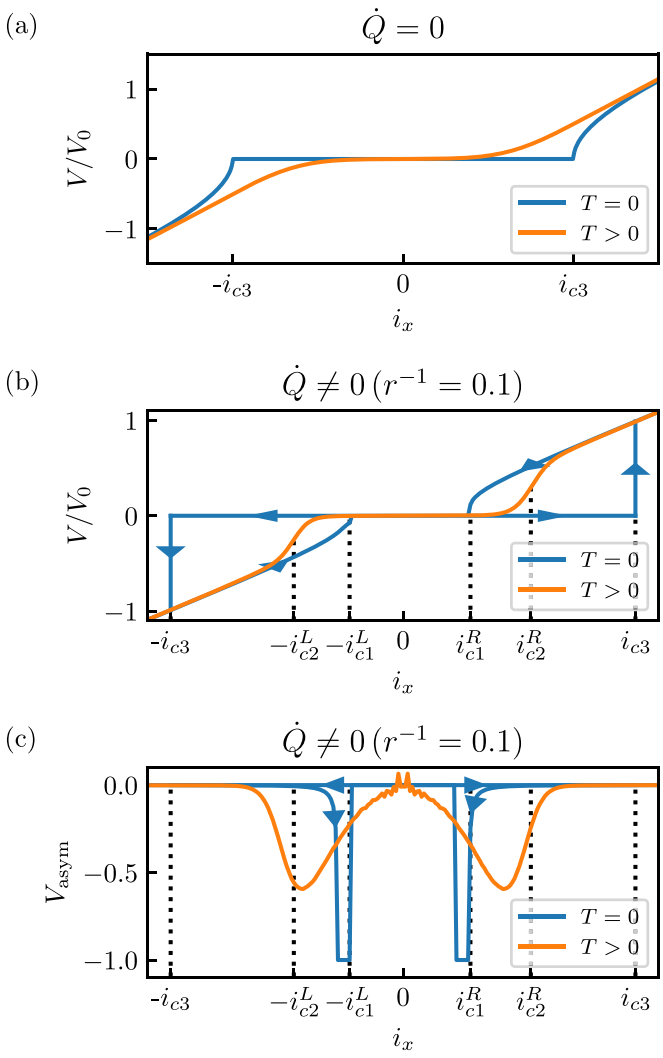


FIG. 2. $I_x$-$V$ characteristic for case (I) at $T=0$ and $T>0$. $I_x$-$V$ characteristic, numerically calculated from Eqs. (8) and (9), for the system (a) without $\dot{Q}$ term and (b), (c) with $\dot{Q}$ term [for the definition of $r^{-1}$, see Eq. (8)], where $i_x=I_x/I_c$ and $V_0=RI_c$ with $I_c=2eE_J/\hbar$. In (c), we show $V_{\rm asym}(i_x)=[V(i_x)+V(-i_x)]/[V(i_x)-V(-i_x)]$ which quantifies the degree of nonreciprocity calculated from the $I_x$-$V$ characteristic (b). We note that $V_{\rm asym}=0$ identically for the $I_x$-$V$ characteristic (a), i.e., when $\dot{Q}=0$. The arrows on blue curves in (b) and (c) represent the directions of the sweep of $i_x$. $i_{c1}$ and $i_{c3}$ are the critical currents at $T=0$, and $i_{c2}$ is the critical current at $T>0$ [27]. To obtain the orange curves ($T>0$ data), we numerically solved the Langevin equation, Eqs. (8) and (9) with stochastic Heun's scheme [28], with the parameters $\tilde{T}=0.25$, $A=0.6$, and $A'=0.3$.

of $Q$ are asymmetric. The asymmetry of the Zener tunneling in the presence of the nonlinear interaction was discussed in Ref. [21], but in their case, the asymmetry is between the tunneling processes from the ground state to the excited state and from the excited state to the ground state. In our case, the tunneling process from the lowest band to the next lowest band for the positive and negative biases are asymmetric.

In the present paper, we study theoretically the nonreciprocal nature of $I_x$-$V$ characteristic of the asymmetric Josephson junction, which is modeled by the asymmetric charging energy $E_{ch}(Q)(\neq E_{ch}(-Q))$. We will show that, both for case (I) and case (II), the asymmetry of $E_{ch}(Q)$ leads to the nonreciprocity.

Before getting into the detailed analysis, here we discuss the origin of the asymmetric charging energy. The capacitance of the junction system originates from two contributions: One is the classical capacitance, determined by the electrostatic energy inside the thin film, and the other is the quantum capacitance, which depends on the charge response properties of two sandwiching bulk superconductors [22–26]. Among these two contributions, the latter one is in general nonlinear and asymmetric when the bulk superconductors exhibit different charge response properties. In Sec. III, we will estimate the order of the quantum capacitance in real systems and discuss how to experimentally measure the nonreciprocity.

## II. RESULTS

### A. Model for case (I)

The DC Josephson effect is described by constant $\varphi$ and $Q=V=0$, where $\varphi$ is determined by $I_x=\frac{2eE_J}{\hbar}\sin\varphi=I_c\sin\varphi$. For $|I_x|>I_c$, there is no solution of the Josephson equation with constant $\varphi$, and because of the Josephson relation, Eq. (3), the voltage $V$ appears. In this picture, $I_c$ is identical for both directions, while one needs to solve the dynamics, i.e., the time dependence, of $Q$ and $\varphi$ when finite voltage appears. In this case, the functional form of $E_{ch}(Q)$, which is related to the voltage $V$ by $V=\frac{\partial E_{ch}}{\partial Q}$, is important. Often the form $E_{ch}(Q)=Q^2/(2C)-V_gQ$ is taken with $C$ being the capacitance and $V_g$ the gate voltage, which induces the chemical potential bias across the junction. The gate voltage term seems to break the symmetry between right and left, i.e., $Q$ and $-Q$, but the shift in the origin of $Q$ recovers that symmetry. Therefore, the essential asymmetry between right and left comes from the higher order terms in $Q$ such as

$$E_{ch}=\frac{Q^2}{2C}+\alpha Q^3+\alpha' Q^4, \tag{6}$$

where $\alpha\neq 0$ for junctions where bulk superconductors exhibit different charge response properties [25,26] (see Sec. III A for details). $\alpha Q^3$ term breaks the inversion symmetry $\mathcal{P}$ and leads to the nonreciprocal response. Here, the term $\frac{Q^2}{2C}$ comes from the classical charging energy, while the term $\alpha Q^3+\alpha' Q^4$ originates from the charging energy of the electromagnetic field penetrating into the bulk superconductors and is known as "quantum capacitance" [22–26]. Then we consider the generalized Josephson equation given as

$$\frac{\hbar}{2e}\dot{\varphi}=\frac{\partial E_{ch}}{\partial Q},\quad \dot{Q}=I_x+\tilde{I}(t)-I_c\sin\varphi-\frac{1}{R}\frac{\partial E_{ch}}{\partial Q}, \tag{7}$$

where we added the fluctuating current $\tilde{I}(t)$ satisfying $\langle\tilde{I}(t)\tilde{I}(t')\rangle=2(\beta R)^{-1}\delta(t-t')$, to include the finite temperature effect.

It is useful to rewrite Eqs. (6) and (7) with the dimensionless parameters $\tilde{\imath}=\tilde{I}/I_c$, $i_x=I_x/I_c$, $r^{-1}=R^{-1}\sqrt{\hbar/(2eCI_c)}$, $A=\alpha C^{3/2}\sqrt{E_J}$, $A'=\alpha' C^2 E_J$, and $\tilde{T}^{-1}=E_J\beta$. Also, we rescale $t$ and $Q$ as $\tau=t\sqrt{2eI_c/(\hbar C)}$ and $q=\sqrt{2e/(\hbar CI_c)}Q$.

Then, Eqs. (6) and (7) can be transformed as

$$\frac{d\varphi}{d\tau} = \frac{\partial \epsilon_{ch}}{\partial q}, \quad \frac{dq}{d\tau} = i_x + \tilde{i}(t) - \sin\varphi - r^{-1}\frac{\partial \epsilon_{ch}}{\partial q}, \tag{8}$$

where

$$\epsilon_{ch} = \frac{q^2}{2} + Aq^3 + A'q^4. \tag{9}$$

Here we note the relationship of the dimensionless parameters defined above to the parameters used in the literature [17]: $r^2 = \beta_c$, where $\beta_c$ is the Stewart-McCumber parameter; $\tau = \omega_p t$ and $q = I_c^{-1}\omega_p Q$, where $\omega_p$ is the plasma frequency of the Josephson circuit. Here, let us discuss the analogy of the dynamical system described by Eqs. (8) and (9) with the particle motion under the periodic potential. The Josephson phase $\varphi$ corresponds to the position $x$, while the charge transfer $q$ corresponds to the momentum $p$. In this particle picture, the potential energy is $-\cos x$ and the kinetic energy is $\epsilon_{ch}(q \to p)$. In this sense, one can define the "time-reversal symmetry" $\mathcal{T}'$ and "inversion symmetry" $\mathcal{P}'$ as

$$\mathcal{T}' : x \to x, p \to -p,$$
$$\mathcal{P}' : x \to -x, p \to -p. \tag{10}$$

Then, our system breaks both $\mathcal{P}'$ and $\mathcal{T}'$, while it preserves $\mathcal{P}'\mathcal{T}'$ except the dissipative term $r^{-1}\frac{\partial \epsilon_{ch}}{\partial q}$ in Eq. (7). Namely, the periodic potential is inversion symmetric, while the kinetic energy is asymmetric with respect to $p$ and $-p$. In the quantum mechanical case, this leads to the asymmetric dispersion $\varepsilon(k) \neq \varepsilon(-k)$.

We will discuss the nonreciprocity of Eq. (8) with Eq. (9) for two cases: First, we will discuss the system with no thermal fluctuation, at $T = 0$. For $|i_x| > 1$, where the bias is so strong that the potential barrier disappears, the dynamics is characterized by the limit cycle in $(\varphi, q)$ space. For $|i_x| < 1$ and sufficiently small $r^{-1}$, there coexists the stable fixed point and the limit cycle, which represents the metastable steady state [29,30]. Secondly, we will discuss the system with thermal fluctuation at finite temperature $T > 0$, where the phase slip is caused by the thermal fluctuation [31,32]. In both cases, we will show that the asymmetry of the charging energy leads to the nonreciprocity.

Here we note that, since the voltage drop $V$ in the presence of $A$ satisfies $V(A, -i_x) = -V(-A, i_x)$, the nonreciprocity characterized by $V_{\rm asym} = [V(A, i_x) + V(A, -i_x)]/[V(A, i_x) - V(A, -i_x)]$ can be rewritten as $[V(A, i_x) - V(-A, i_x)]/[V(A, i_x) + V(-A, i_x)]$, so we calculate the voltage drop $V(A, i_x)$ for positive $i_x$ and change the sign of $A$. For the same reason, $i_{c1}^R(-A) = i_{c1}^L(A)$. From now on, we fix the parameters $A = \pm 0.6$ and $A' = 0.3$ for the purpose of demonstration of the asymmetry. We will discuss the estimation of these parameters in real materials in Sec. III A.

### B. Nonreciprocal $I_x$-$V$ characteristic at $T = 0$ for case (I)

In Fig. 2 (blue curves), we show the $I_x$-$V$ characteristic, numerically calculated from Eqs. (6) and (7) without the $\dot{Q}$ term (panel a) and with $\mathcal{P}$ breaking $\dot{Q}$ term (panel b) at $T = 0$. As we mentioned in the introduction, the nonreciprocity is realized only for the latter system, see panel c.

An important feature of $I_x$-$V$ characteristic at $T = 0$ with finite $\dot{Q}$ [Fig. 2(b), blue curve] is the hysteresis for $i_{c1}^R < i_x < i_{c3}$ and $-i_{c3} < i_x < -i_{c1}^L$. This hysteresis comes from the coexistence of the limit cycle and stable fixed point [29,30]. As can be seen from Figs. 3(b) and 3(c), because of the presence of the limit cycle, for the initial condition inside the dark blue region, the longtime dynamics is governed by the limit cycle so that the voltage drop is finite. On the contrary, for the initial condition inside the green region, the particle is attracted to the stable fixed point and the voltage drop is zero. Sweeping $i_x$ from the large value to the small value corresponds to the former case, while sweeping $i_x$ from the small value to the large value corresponds to the latter case. Namely, the hysteresis behavior occurs. On the contrary, there is no hysteresis for $I_x$-$V$ characteristic at $T = 0$ without $\dot{Q}$ term [Fig. 2(a), blue curve].

Here we review the qualitative aspect of the bifurcation of the limit cycle in the system with $T = 0$ [29,30] for $i_x > 0$. The system shows qualitatively different behavior depending on the value of the dimensionless dissipation strength $r$, defined above Eq. (8).

For $r^{-1} \gg 1$ [Fig. 2(a)], we can neglect the inertia term (the capacitance term, $dq/d\tau$) and Eq. (8) becomes

$$r^{-1}\frac{d\varphi}{d\tau} = i_x - \sin\varphi. \tag{11}$$

For $i_x > 1$, $d\varphi/d\tau > 0$ and there is only a limit cycle [Fig. 4(c)]. As we decrease $i_x$, at $i_x = i_{c3} = 1$, the saddle-node

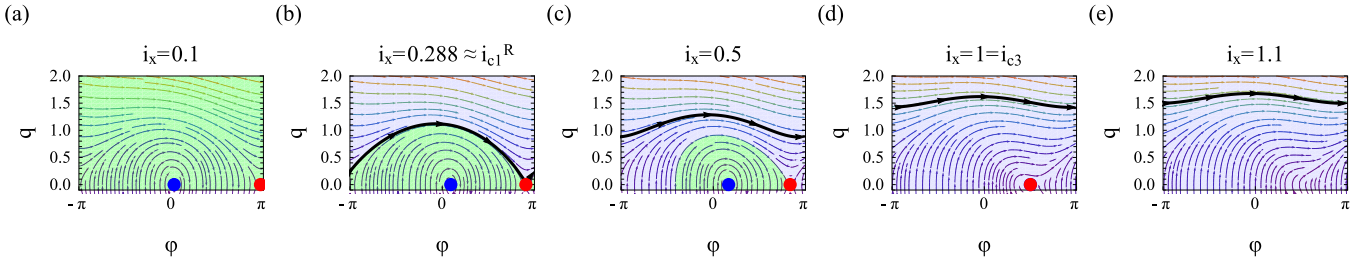


FIG. 3. The bifurcations of the system with finite capacitance, Eqs. (8) and (9). We set $A = 0.6$, $A' = 0.3$, $r^{-1} = 0.1$ and (a) $i_x = 0.1$, (b) $i_x = 0.288 \cong i_{c1}^R$, (c) $i_x = 0.5$, (d) $i_x = 1 = i_{c3}$, and (e) $i_x = 1.1$. The blue and red dots represent the stable fixed point and saddle point, respectively. Black curves represent the (meta)stable limit cycles, and the green and dark blue regions are the basins of attraction of the stable fixed point (blue dot) and limit cycle (black curve), respectively. We present the case of positive $i_x$. While the behavior is similar also for $i_x < 0$, the critical $i_{c1}^L$ is different from $i_{c1}^R$.

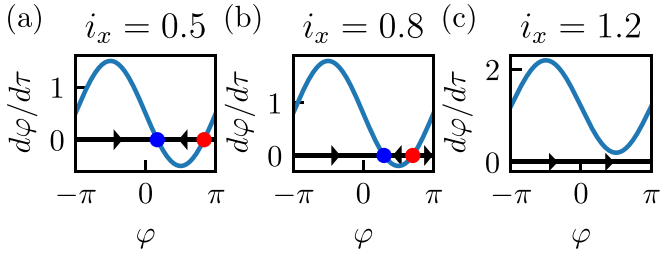


FIG. 4. The bifurcation of the system with $\dot{Q} = 0$, i.e., Eq. (11), for (a) $i_x = 0.5$, (b) $i_x = 0.8$, and (c) $i_x = 1.2$. The blue curve represents the value of $d\varphi/d\tau$ at each $\varphi$, and the arrow on the black curve represents the direction of the velocity. The blue and red dots represent the stable fixed point and saddle point, respectively. We can see that there is no limit cycle for $i_x < 1$.

(blue-sky) bifurcation leads to the vanishing of the limit cycle and the birth of the stable and unstable fixed points at $\varphi = \sin^{-1} i_x$ and $\pi - \sin^{-1} i_x$, respectively, see Figs. 4(b) and 4(c). For $i_x < 1$, the longtime dynamics is governed by the stable fixed point, see Figs. 4(a) and 4(b). Therefore, for $r^{-1} \gg 1$, the disappearance of the limit cycle and the birth of the stable fixed point occur simultaneously, i.e., $i_{c1}^R = i_{c3} = 1$. Above $i_{c3}$, the flow of $\varphi$ occurs, and we get the finite time-averaged voltage drop $\bar{V} = \mathrm{sign}(I_x)R\sqrt{I_x^2 - I_c^2}$ as we mentioned in the introduction.

For $r^{-1} \ll 1$ [Fig. 2(b)], we cannot neglect the inertia term in Eq. (8), and, although the longtime dynamics for $i_x > i_{c3} = 1$ is governed by the limit cycle just as in the $r^{-1} \gg 1$ case, the system exhibits *two* bifurcations as we decrease $i_x$. One is at $i_x = i_{c3} = 1$, where the saddle-node bifurcation leads to the birth of the stable fixed point and the saddle point at $(\varphi, q) = (\sin^{-1} i_x, 0)$ and $(\pi - \sin^{-1} i_x, 0)$, as is shown in Figs. 3(c), 3(d) and 3(e). The other one is the homoclinic bifurcation at $i_x = i_{c1}^R$, where the limit cycle collides with the saddle point at $(\varphi, q) = (\pi - \sin^{-1} i_x, 0)$ to become the homoclinic orbit and then disappears, as is shown in Figs. 3(a) and 3(b). We will review what a homoclinic orbit is and discuss its role

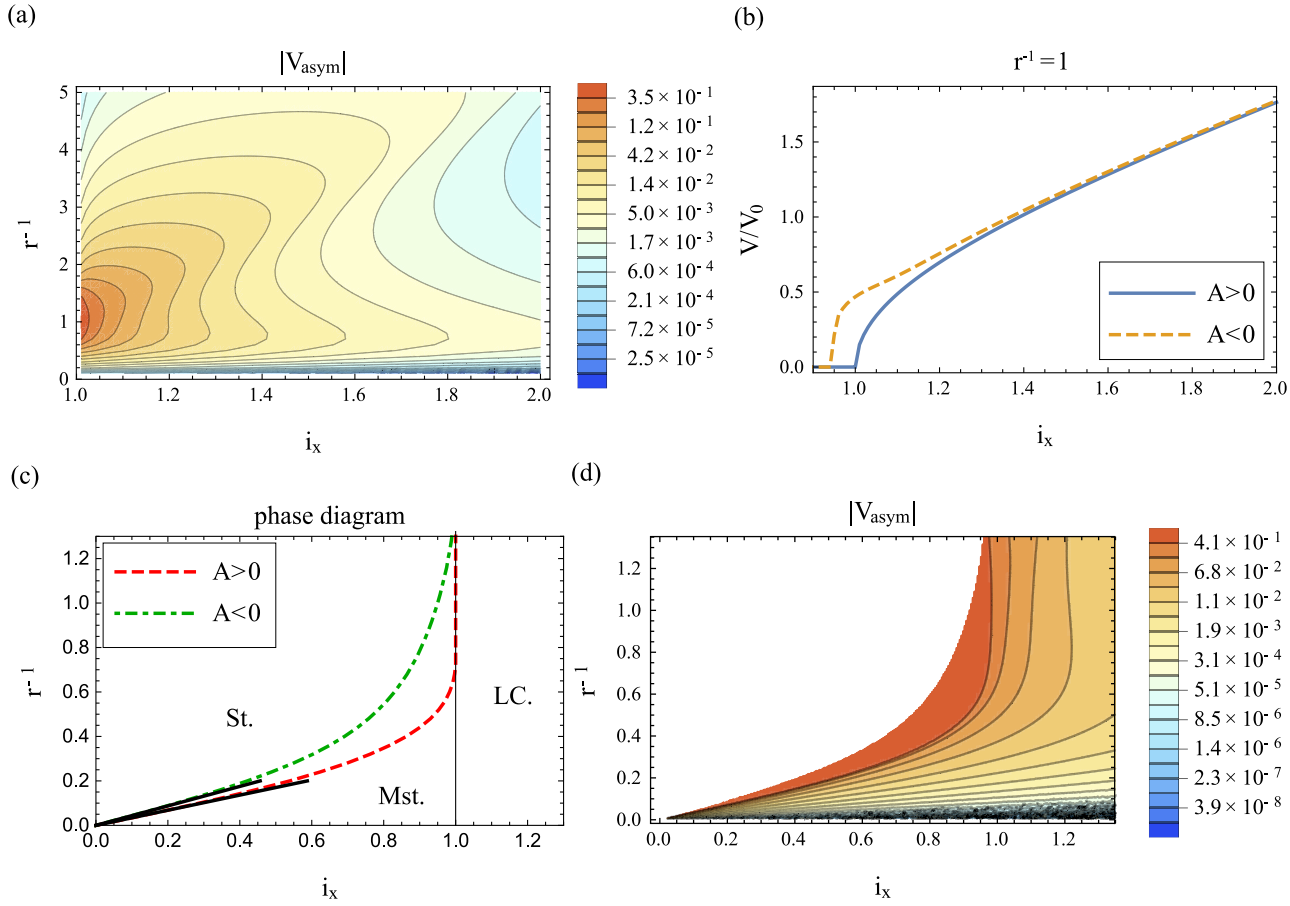


FIG. 5. Nonreciprocity for various $i_x$ and $r^{-1}$ for case (I) at $T = 0$. (a) $V_{\mathrm{asym}}(i_x) = [V(i_x) + V(-i_x)]/[V(i_x) - V(-i_x)]$ as a function of $i_x$ and $r^{-1}$, numerically calculated from Eqs. (8) and (9) with $\tilde{T} = 0$. (b) The voltage drop $V/V_0$ where $V_0 = RI_c$ for $A > 0$ and $A < 0$ with $r^{-1} = 1$ and $\tilde{T} = 0$ in Eqs. (8) and (9). (c) The phase diagram in $(i_x, r^{-1})$ space for the dynamical system governed by Eqs. (8) and (9) with $\tilde{T} = 0$. St., Mst. and LC. represent the phase with the stable fixed point only, stable fixed point coexisting with the limit cycle, and limit cycle only, respectively. The black curves are the phase boundaries calculated from Eq. (12). (d) $V_{\mathrm{asym}}(i_x)$ near the phase boundary, where $V(i_x)$ is calculated for the metastable limit cycle of Eqs. (8) and (9) with $\tilde{T} = 0$, i.e., the plot corresponds to the sweeping of $i_x$ from the large value in Fig. 2(b). In the white region, $V = 0$ for both $A > 0$ and $A < 0$ cases, while in the region where $|V_{\mathrm{asym}}| = 1$, $V \neq 0$ for $A > 0$ and $V = 0$ for $A < 0$. Therefore, the step of $|V_{\mathrm{asym}}|$ comes from the difference of the critical current for $A > 0$ and $A < 0$. We note that $V_{\mathrm{asym}} < 0$ for the parameter region shown in (a) and (d).

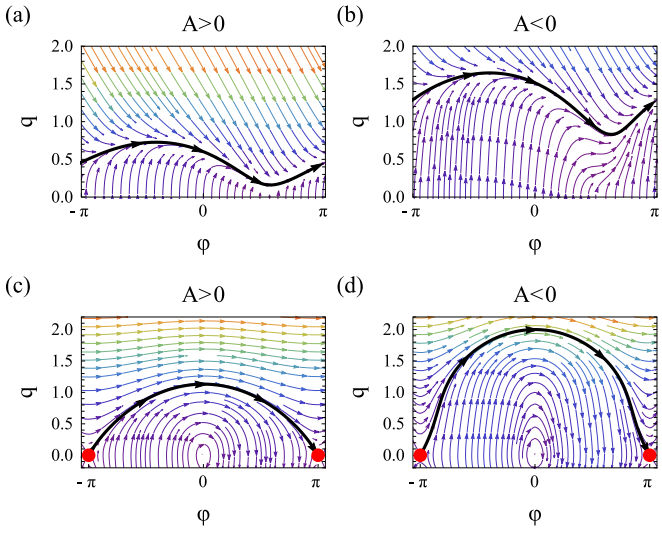


FIG. 6. (a),(b) The limit cycles for $i_x > 1$ and (c),(d) the homoclinic orbits for $i_x = r^{-1} = 0$. (a),(b) The limit cycles, shown by black curves, for Eqs. (8) and (9) with $i_x = 1.2$, $r^{-1} = 1$, where (a) $A > 0$ and (b) $A < 0$. (c),(d) The homoclinic orbits, shown by black curves, for Eqs. (8) and (9) with $r^{-1} = i_x = 0$ where (c) $A > 0$ and (d) $A < 0$. The red dots represent the fixed points. Note that $(\varphi, q) = (\pi, 0)$ and $(-\pi, 0)$ are equivalent.

in the phase diagram later. As for the bifurcations for $i_x < 0$, the qualitative nature of the bifurcations is the same, but importantly, $i_{c1}^L \neq i_{c1}^R$ because of the asymmetry of the charging energy. It leads to the enhancement of $V_{\rm asym}$ near $-i_{c1}^L$ and $i_{c1}^R$ as can be seen in Fig. 2(c).

### C. Nonreciprocity for various $i_x$ and $r^{-1}$ at $T = 0$ for case (I)

For $|i_x| > 1$, $V_{\rm asym}$ as a function of $i_x$ and $r^{-1}$ is shown in Fig. 5(a). We can see that the nonreciprocity is enhanced for small $i_x$ and $r^{-1}$. Since $|i_x| > 1$, the longtime dynamics is governed by the limit cycle traversing from $\varphi = -\pi$ to $\pi$ at finite $q$ as is shown in Figs. 6(a) and 6(b). As we can see from these figures, the limit cycles for $A > 0$ and $A < 0$ are different, so that $V_{\rm asym}$ is finite.

For $|i_x| < 1$, the homoclinic bifurcation occurs at $i_{c1}^R$ and $-i_{c1}^L$. As we explained, at this bifurcation point the limit cycle becomes the homoclinic orbit. In short, a homoclinic orbit is a variant of a limit cycle. However, in contrast to a limit cycle, there is a fixed point on it, so its time period is infinite, since it takes infinite time to reach and depart from the fixed point. For example, the black curves in Figs. 3(b) and 6(c) and 6(d) are homoclinic orbits where the fixed point is shown by the red dots. Since the presence of the homoclinic orbit indicates the homoclinic bifurcation, by identifying the one-parameter family of the homoclinic orbit on the $(i_x, r^{-1})$ plane, we can calculate $i_{c1}^{R/L}$ as a function of $r^{-1}$.

For small $i_x$ and $r^{-1}$, we can perturbatively calculate $i_{c1}^{R/L}$ from the parameter $i_x = r^{-1} = 0$, where we can analytically calculate the homoclinic orbit, see Figs. 6(c) and 6(d). $i_{c1}^{R/L}(r^{-1})$ can be calculated from the simple zero of the following Melnikov function [33]:

$$\int_{-\infty}^{\infty} dt \dot{\varphi}_0(t)(i_x - r^{-1}\dot{\varphi}_0(t)) = 2\pi i_x - 2r^{-1}\int_0^{q_{\rm max}} dq \left(\frac{d\epsilon_{ch}(q)}{dq}\right)^2 \frac{1}{\sqrt{\epsilon_{ch}(q)[2-\epsilon_{ch}(q)]}}, \tag{12}$$

where $\varphi_0(t)$ is the homoclinic orbit for $i_x = r^{-1} = 0$ shown in Figs. 6(c) and 6(d), and $q_{\rm max}$ is the maximum of $q$ along that orbit. As we can see, the homoclinic orbits for $A > 0$ [Fig. 6(c), black curve] and $A < 0$ [Fig. 6(d), black curve] are very different and that leads to the difference of the Melnikov functions in two cases, so that $i_{c1}^L(r^{-1}) \neq i_{c1}^R(r^{-1})$. In Fig. 5(c), we show the phase boundary [i.e., $i_{c1}^{R/L}(r^{-1})$] obtained from the direct numerical calculation (red dotted and green dot-dashed curves) and the one obtained from the condition that Eq. (12) should be zero (black solid curve). We can see that the prediction of Eq. (12) agrees well with the numerically obtained boundary for small $i_x$ and $r^{-1}$. For $(i_x, r^{-1})$ such that metastable limit cycle does exist for $A < 0$ but not for $A > 0$, we observe $|V_{\rm asym}| = 1$, i.e., the perfect nonreciprocity, as is shown in Fig. 5(d), since the time-averaged velocity $\overline{d\varphi/d\tau} \propto \bar{V} = 0$ for $A > 0$, while $\overline{d\varphi/d\tau} \propto \bar{V} \neq 0$ for $A < 0$. We also note that the large $|V_{\rm asym}|$ for $i_x \gtrsim 1$ [Fig. 5(a)] can be understood as a consequence of the difference of $i_{c1}^R$ and $i_{c1}^L$: As we can see from Fig. 5(b), the voltage drop $V$ is larger for $i_x \gtrsim 1$ for $A < 0$, because $i_{c1}$ is smaller for $A < 0$.

### D. Nonreciprocal $I_x$-$V$ characteristic at finite temperature $T > 0$ for case (I)

For the finite temperature $T > 0$ case, we numerically solved the Langiven equation, Eq. (8), with stochastic Heun's scheme [28] to calculate the physical quantities and then took an ensemble average. Numerically calculated $I_x$-$V$ characteristic is shown in Fig. 2 (orange curves). As is shown in Fig. 2(b), we can see that the voltage drop $V$ suddenly increases around $i_{c2}^R$ and $-i_{c2}^L$ and merges to the curve $V/V_0 = i_x$. This behavior can be understood as the dynamical transition, from the state where the dominant probabilistic weight is on the stable fixed point so that the voltage drop is around zero, to the one where the limit cycle is primarily realized and the finite voltage drop results [27,34]. Since the system is at the finite temperature, the transition is not sharp, but as $T \to +0$ this transition becomes sharper and the jump of $V$ from 0 to finite value occurs at $i_x = i_{c2}^R$ and $-i_{c2}^L$ when $T = +0$. At the same time, the relaxation time between the two configurations diverges as $T \to +0$, and when the experimental measurement time is smaller than the relaxation time, we observe the hysteresis behavior as we discussed above for the $T = 0$ case. In a similar manner to the $T = 0$ case, the large $V_{\rm asym}$ near $i_{c2}^R$ and $-i_{c2}^L$ is realized, since $i_{c2}^R \neq i_{c2}^L$.

### E. Nonreciprocity for various $i_x$ and $r^{-1}$ at $T > 0$ for case (I)

Just as in the $T = 0$ case, we numerically solved Eq. (8) to calculate the nonreciprocity for various $i_x$ and $r^{-1}$ with $T > 0$, and the result of the numerical calculation is shown in Fig. 7. As we can see, the nonreciprocity is enhanced for

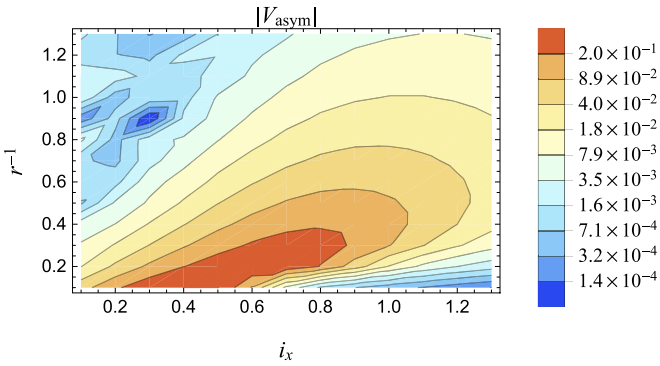


FIG. 7. Nonreciprocity for various $i_x$ and $r^{-1}$ for case (I) at $T > 0$. $V_{\rm asym}(i_x) = [V(i_x) + V(-i_x)]/[V(i_x) - V(-i_x)]$ at $T > 0$. For the parameter region shown in the plot, $V_{\rm asym} < 0$. We numerically solved Eqs. (8) and (9) with $\tilde{T} = 0.25$. The jaggy result of $|V_{\rm asym}|$ for the small $|V_{\rm asym}|$ region ($|V_{\rm asym}| \lesssim 10^{-3}$) comes from the numerical error of the Langevin equation. We note that the relative error of $|V_{\rm asym}|$ is small for large $|V_{\rm asym}|$ region ($|V_{\rm asym}| \gtrsim 10^{-2}$), and we focus only on this region in the present paper.

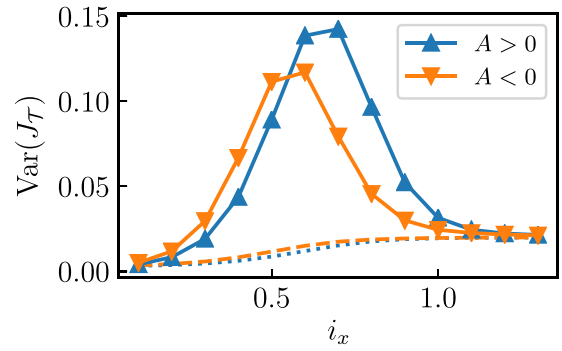


FIG. 9. Variance of $J_\mathcal{T}$ for case (I) at $T > 0$. The blue dotted and orange dashed curves are the lower bound predicted by the thermodynamic uncertainty relation, $\mathrm{Var}(J_\mathcal{T}) \geqslant 2\langle J_\mathcal{T}\rangle^2/(\mathcal{T}\sigma)$, where $\sigma$ is the entropy production rate and is calculated as $\sigma = i_x\langle J_\mathcal{T}\rangle/\tilde{T}$ [35]. We numerically solved the Langevin equation (8) and (9) for 100 ensembles with time $\tau = 10^7$ and $\Delta\tau = 10^{-2}$ by the stochastic Heun's scheme [28] and set $\mathcal{T} = 1000$. The parameters are set to be $r^{-1} = 0.1$ and $\tilde{T} = 1$.

small $r^{-1}$, i.e., small dissipation, region. This is consistent with the fact that, for $r^{-1} \gg 1$, we can neglect the inertia term in Eq. (8) to obtain the usual inversion-symmetric overdamped Langevin equation. In addition, we can see the peak structure at finite value of $i_x$ for fixed $r^{-1}$. To understand this behavior, it is useful to plot the normalized mobility $r^{-1}\mu = V/(V_0 i_x)$, where $V_0 = RI_c$, as a function of $i_x$ [34], see Fig. 8(a). We can see that for small $i_x$, the mobility is almost zero, but at some finite $i_x$ the mobility jumps to $\mu = r$ and saturates. This kind of behavior can be understood from $W_\pm(E)$, which is defined from the distribution function of the energy as

$$P(E) = \begin{cases} \mathcal{N}e^{-W_+(E)/\tilde{T}} & (q \geqslant 0) \\ \mathcal{N}e^{-W_-(E)/\tilde{T}} & (q < 0) \end{cases}, \quad E = \epsilon_{ch}(q) - \cos\varphi, \quad (13)$$

where $P(E)$ is the distribution function of $E$, and we introduced two functions $W_+$ and $W_-$, corresponding to the two branches of momentum $q$ as a function of the energy $E$ [34]. Numerically calculated $W_+(E)$ for $A > 0$ and $A < 0$ is shown in Figs. 8(b) and 8(c). We can see that, as we increase the bias $i_x$, $W_+(E)$ at large $E$ becomes small and eventually the local minimum at $E > 1$ drops below the value at $E = -1$. This corresponds to the dynamical transition of the typical trajectory from the static one at $E = -1$ to the running one at $E > 1$. We can see that the critical value of $i_x$ which we denote $i_{c2}$, where this transition occurs, is different for the $A > 0$ case ($i_{c2} \sim 0.6$) and $A < 0$ case ($i_{c2} \sim 0.5$). The fact that $i_{c2}$ is larger for $A > 0$ is consistent with the larger $i_{c1}$ where the limit cycle emerges, as is shown by blue dot-dashed and orange dashed lines in Fig. 8(a).

Because of the presence of the thermal fluctuation, we can discuss not only the average value of the velocity, but also the whole distribution of the time-averaged current $J_\mathcal{T} = \int_0^\mathcal{T} d\tau \frac{d\varphi}{d\tau}$ [35]. The numerically calculated variance of $J_\mathcal{T}$ is shown in Fig. 9. Since the system does not have $\mathcal{T}'$ symmetry, we might have a violation of the lower bound of the variance known as thermodynamic uncertainty relation [35–37], as is observed in the underdamped Langevin system with magnetic field [38], but we did not observe any violation for the parameter region we have calculated. As we can see, the fluctuation of $J_\mathcal{T}$ becomes large for intermediate $i_x$. This reflects the fact that there coexists the stationary trajectory and the running trajectory, and these two trajectories, which have quite different average velocities, are probabilistically realized, leading to the large fluctuation of the current. For larger $i_x$ the fluctuation de-

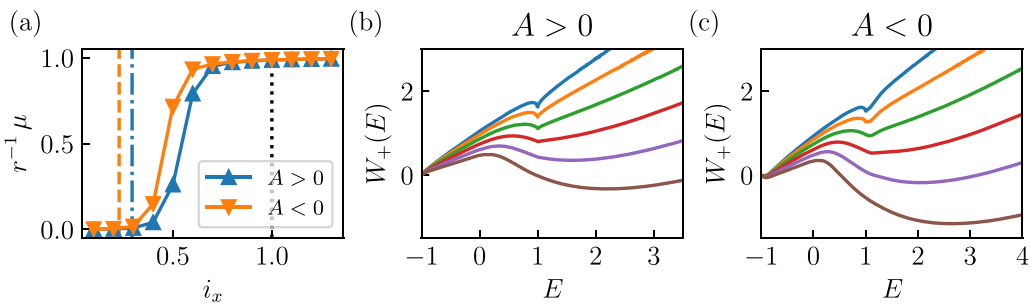


FIG. 8. Normalized mobility and the distribution function of energy for case (I) at $T > 0$. (a) Normalized mobility $r^{-1}\mu$, where $r^{-1}\mu = V/(V_0 i_x)$ and $V_0 = RI_c$, as a function of $i_x$ for $r^{-1} = 0.1$. The value where the limit cycle appears is shown by the dot-dashed blue and the dashed orange curves, and the value where the stable fixed point vanishes is shown by black dotted curve. (b),(c) $W_+(E)$, defined in Eq. (13) at $r^{-1} = 0.1$, from $i_x = 0.1$ (blue curve) to $i_x = 0.6$ (brown curve), where (b) $A > 0$ and (c) $A < 0$. We set $\tilde{T} = 0.25$ in Eqs. (8) and (9).

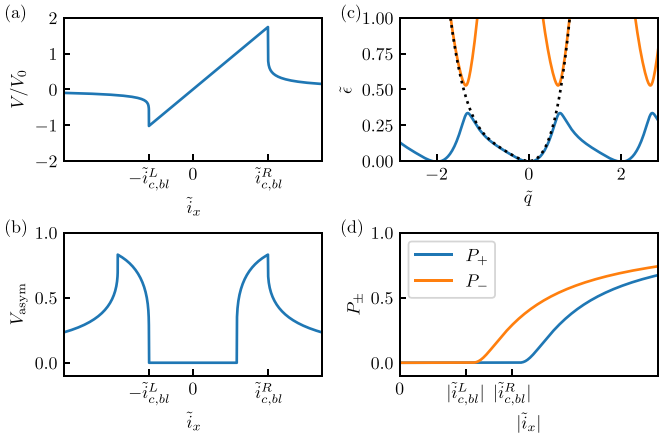


FIG. 10. $I_x$-$V$ characteristic, energy dispersion, and nonreciprocal Zener tunneling for case (II). (a) $I_x$-$V$ characteristic and (b) $V_{\rm asym}(\tilde{i}_x) = [V(\tilde{i}_x) + V(-\tilde{i}_x)]/[V(\tilde{i}_x) - V(-\tilde{i}_x)]$, calculated from Eqs. (18) and (19), where $V_0 = e/C$. (c) Energy dispersion of the two lowest energy bands with the asymmetric changing energy $E'_{ch}(\tilde{q}) = \tilde{q}^2/2 + \tilde{A}\tilde{q}^3 + \tilde{A}'\tilde{q}^4$ with $\tilde{A} = 0.6$ and $\tilde{A}' = 0.3$, and we set $E_J/E_Q = 0.2$, where $E_Q = e^2/(2C)$, to open up a gap in the spectrum. Dotted curve represents the energy dispersion without the Josephson coupling term $E_J \cos\varphi$ in the Hamiltonian. (d) The LZ rate calculated from Eq. (20) with $E_J/E_Q = 0.1$ ($E_Q = e^2/(2C)$) and $R/R_q = 100$, where $R_q = e^2/(2\pi\hbar)$.

creases, since the stationary fixed point disappears. Reflecting the difference of the critical current $i_{c2}$, the region where the current fluctuation enhances is different for $A > 0$ and $A < 0$ cases, and that leads to quite different current fluctuation as we can see in Fig. 9.

### F. Model for case (II)

As we mentioned in the introduction, the dynamics in this case is governed by Eq. (5), and $E_J/E_Q$ characterizes the ratio of the band gap to the bandwidth, see Fig. 10(c). In this case, because of the periodicity of the Brillouin zone, the system exhibits the Bloch oscillation, which affects the $I_x$-$V$ characteristic in a substantial way [20,39]. Physically, the Bloch oscillation in $Q$ space corresponds to the cooper pair tunneling through the Josephson junction [20], and it reduces the current flowing through the resistive channel of the junction, so the voltage drop $V$ is suppressed. The Bloch oscillation is hindered by the Zener tunneling process where the state is excited to higher energy bands, and $I_x$-$V$ characteristic is determined by the competition between the Bloch oscillation and the Zener tunneling [39–41].

For the discussion of the Bloch oscillation, for simplicity, we work in the lowest order approximation in $E_J$, i.e., we neglect the gap at the Brillouin zone boundary but assume the periodic structure of the energy dispersion, $\tilde{E}_{ch}$, i.e.,

$$\tilde{E}_{ch}(Q) = \min_{n\in\mathbb{Z}} E_{ch}(Q - 2ne). \tag{14}$$

Setting $Q = e\tilde{q}$, $t = RC\tilde{\tau}$, $I_x = \tilde{i}_x e/(RC)$, Eq. (5) becomes

$$\frac{d\tilde{q}}{d\tilde{\tau}} = \tilde{i}_x - \frac{\partial\tilde{\epsilon}}{\partial\tilde{q}}, \tag{15}$$

where

$$\tilde{\epsilon}(\tilde{q}) = \min_{n\in\mathbb{Z}} E'_{ch}(\tilde{q} - 2n), \quad E'_{ch}(\tilde{q}) = \frac{\tilde{q}^2}{2} + \tilde{A}\tilde{q}^3 + \tilde{A}'\tilde{q}^4, \tag{16}$$

where $\tilde{A} = \alpha Ce$, $\tilde{A}' = \alpha' Ce^2$. We set $\tilde{A} = 0.6$ and $\tilde{A}' = 0.3$ for the purpose of illustration. See Sec. III A for the estimation of these parameters in real systems.

### G. Nonreciprocal Bloch oscillation for case (II)

First, we will discuss the nonreciprocity of the Bloch oscillation in the Josephson junction. For the energy dispersion (16), denoting the left and right Brillouin zone boundary by $\tilde{q}_{L,R}$, the conditions for the Bloch oscillation to occur for $\tilde{i}_x > 0$ and $\tilde{i}_x < 0$ cases can be calculated as

$$\tilde{i}_x \geqslant \frac{\partial\tilde{\epsilon}(\tilde{q}_R)}{\partial\tilde{q}} =: \tilde{i}^R_{c,bl}, \quad \tilde{i}_x \leqslant \frac{\partial\tilde{\epsilon}(\tilde{q}_L)}{\partial\tilde{q}} =: -\tilde{i}^L_{c,bl}, \tag{17}$$

respectively. The periods of the Bloch oscillation for $\tilde{i}_x > 0$ and $\tilde{i}_x < 0$ cases are

$$\tilde{\tau}_R = \int_{\tilde{q}_L}^{\tilde{q}_R} \frac{d\tilde{q}}{\tilde{i}_x - \frac{\partial\tilde{\epsilon}}{\partial\tilde{q}}}, \quad \tilde{\tau}_L = \int_{\tilde{q}_R}^{\tilde{q}_L} \frac{d\tilde{q}}{\tilde{i}_x - \frac{\partial\tilde{\epsilon}}{\partial\tilde{q}}}. \tag{18}$$

Then, the voltage drop can be derived from Eq. (15) as [20]

$$V_{L,R} = \frac{e}{C}\left\langle\frac{\partial\tilde{\epsilon}}{\partial\tilde{q}}\right\rangle = \frac{e}{C}\left(\tilde{i}_x - \frac{2}{\tilde{\tau}_{L,R}}\right). \tag{19}$$

We show the voltage drop calculated from Eqs. (18) and (19) in Figs. 10(a) and 10(b). As we can see, since the critical currents where the Bloch oscillation sets in are different for $\tilde{i}_x > 0$ and $\tilde{i}_x < 0$, i.e., $\tilde{i}^R_{c,bl} \neq \tilde{i}^L_{c,bl}$, $I_x$-$V$ characteristic exhibits nonreciprocity.

### H. Nonreciprocal Zener tunneling for case (II)

Next, we discuss the nonreciprocity in the Zener tunneling rate. The general expression of the Zener tunneling rate is derived in Ref. [40], where the argument is only for the quadratic charging energy. Generalizing their argument to include the asymmetry of the charging energy, we obtain

$$P_\pm = \exp\left[-\left(\frac{\pi E_J}{2E_Q}\right)^2 \frac{R}{R_q}\frac{1}{|V_{C,\pm}||v_\pm|}\right], \quad \left(R_q = \frac{e^2}{2\pi\hbar}\right), \tag{20}$$

where we neglected the effect of the fluctuation of the charge. Here

$$V_{C,\pm} = \left.\frac{d}{d\tilde{q}}(E'_{\rm ch}(\tilde{q}) - E'_{\rm ch}(\tilde{q} \mp 2))\right|_{\tilde{q}=\tilde{q}_R/\tilde{q}_L},$$

and, as we can easily see, $|V_{C,+}| = |V_{C,-}|$. $v_\pm$ is the velocity of the charge at $\tilde{q}_{R,L}$ given by the solution of Eq. (15), i.e.,

$$v_\pm = \tilde{i}_x - \left.\frac{\partial\tilde{\epsilon}}{\partial\tilde{q}}\right|_{\tilde{q}=\tilde{q}_R/\tilde{q}_L} = \tilde{i}_x \mp \tilde{i}^{R/L}_{c,bl}, \tag{21}$$

where $\tilde{i}^{R/L}_{c,bl}$ are defined in Eq. (17). As we noted $\tilde{i}^R_{c,bl} \neq \tilde{i}^L_{c,bl}$, so $|v_+(\tilde{i}_x)| \neq |v_-(-\tilde{i}_x)|$ and $P_+ \neq P_-$. The Landau-Zener tunneling probability $P_\pm$ obtained from Eq. (20) is shown in Fig. 10(d). We can see the threshold behavior coming from the dissipation [42].

Here we note the importance of the effect of dissipation in obtaining the nonreciprocal Zener tunneling rate. In the present semiclassical approximation, there occurs no quantum tunneling when the classical solution does not reach the band crossing point due to the dissipation. Then the asymmetric threshold current is the origin of the nonreciprocal tunneling rate, and hence the dissipation is required for the nonreciprocity. On the other hand, it is shown in Ref. [2] that the nonreciprocal Landau-Zener tunneling occurs if we have nonzero shift vector even without the dissipation. Here, as we noted before, we are considering the system where $\mathcal{P}'$ and $\mathcal{T}'$ is broken by the asymmetry of the dispersion relation, but the system still has $\mathcal{P}'\mathcal{T}'$ symmetry. Then, from the general transformation rule [4], the shift vector is identically zero. Furthermore, we can show that, in the absence of the shift vector, there is no nonreciprocity in the LZ rate even in the presence of the asymmetry in the band energy for the dissipationless system. To show this, we observe that, in the absence of shift vector, the amplitude for the tunneling process during one cycle of Bloch oscillation under the electric field $E = -E_x < 0$ is given as [2],

$$a_+^{(-E_x)} = ie^{i\arg A_{+-}(-\pi)} \int_{-\pi}^{\pi} dk_1 |A_{+-}|(k_1) e^{-i\int_{-\pi}^{k_1} dk_2 \frac{\Delta(k_2)}{-eE_x}}, \quad (22)$$

where $A_{+-} = \langle u_+|\partial_k|u_-\rangle$, $|u_\pm\rangle$ is the wave function for upper/lower band, and $\Delta(k)$ is the $k$ dependent difference of the upper and lower band energy. Although the standard estimation utilizes the integration path in the complex $k$ plane, here we only consider the integration path on the real $k$ line. From Cauchy's theorem, this does not spoil any generality of our result. Then, the expression for the reverse process with the electric field $E = E_x > 0$ is given as

$$a_+^{(E_x)} = ie^{i\arg A_{+-}(\pi)} \int_{\pi}^{-\pi} dk_1 |A_{+-}|(k_1) e^{-i\int_{\pi}^{k_1} dk_2 \frac{\Delta(k_2)}{eE_x}}.$$

Then, by taking the complex conjugate of Eq. (22), we can show that $(a_+^{(-E_x)})^* = e^{i\chi} a_+^{(E_x)}$, where

$$\chi = -\arg A_{+-}(-\pi) - \arg A_{+-}(\pi) - \int_{-\pi}^{\pi} dk_2 \frac{\Delta(k_2)}{eE_x}.$$

Therefore, we conclude that $|a_+^{(-E_x)}| = |a_+^{(E_x)}|$ in the absence of shift vector, even if the system breaks $\mathcal{P}'$ symmetry. The situation is different if we include the dissipation to the system, as we can see from Eq. (20). Since the semiclassical dynamics of $Q$ reflects the asymmetry of the dispersion through the dissipative term, the nonreciprocal LZ effect is realized.

## III. DISCUSSION

### A. Nonlinear capacitance

Here, we estimate the nonlinear capacitance $\alpha$ [22–26] defined in Eq. (6) using the scaling form derived by the Thomas-Fermi approximation [25,26]:

$$\alpha \propto \left[\frac{(4\pi)^2}{\epsilon_{F,2}}\left(S\lambda_2\lambda_2^{-2}e^{-2}\right)^{-2} - \frac{(4\pi)^2}{\epsilon_{F,1}}\left(S\lambda_1\lambda_1^{-2}e^{-2}\right)^{-2}\right]\frac{1}{e^3},$$
$$\propto \left[\frac{1}{n_2} - \frac{1}{n_1}\right]\frac{4\pi}{eS^2} \quad (23)$$

where $S$ is the area of the cross section of the Josephson junction, $\lambda_{1,2}$ and $n_{1,2}$ are the Thomas-Fermi screening lengths and carrier density of the bulk superconductors, and we replaced the derivative operator $d/d\epsilon$ with $1/\epsilon_F$ ($\epsilon_F$ is the Fermi energy) for the order estimation. From this expression, we can see that $\alpha$ is enhanced for the junctions with largely different values of $n_1$ and $n_2$. From now on, we consider the junctions consisting of a superconductor with small $n_1$, e.g., FeSe, where the carrier density is of the order of $|n_1| \sim 10^{20}$ cm$^{-3}$ [43], and one with larger $n_2$, e.g., a conventional superconductor, where $|n_2| \sim 10^{22}$ cm$^{-3}$. Now, the linear capacitance in the Thomas-Fermi approximation can be written as

$$C = \frac{\epsilon_r}{4\pi}\frac{S}{a+\lambda_1+\lambda_2}, \quad (24)$$

where $\epsilon_r$ and $a$ are the relative dielectric constant and thickness of the thin film, respectively.

First we consider the case (I), where the dynamics is governed by Eqs. (8) and (9). Then, in the dimensionless unit, we get

$$A = \alpha C^{3/2}\sqrt{E_J}$$
$$\propto \left[\frac{\epsilon_r}{n_2 S(a+\lambda_1+\lambda_2)} - \frac{\epsilon_r}{n_1 S(a+\lambda_1+\lambda_2)}\right]\sqrt{\frac{E_J}{2E_Q}}. \quad (25)$$

Now, we set the typical values $\epsilon_r \sim 10$, $S \sim 0.1\ \mu$m$^2$, $a = 1$ nm, $E_Q/E_J \sim 10^{-1}$ and assume $a \gg \lambda_{1,2}$. Then, $A \sim 10^{-3}$.

If we consider the case (II), where the dynamics is governed by Eqs. (15) and (16), in dimensionless unit,

$$\tilde{A} = \alpha C e \sim \left[\frac{\epsilon_r}{n_2 S(a+\lambda_1+\lambda_2)} - \frac{\epsilon_r}{n_1 S(a+\lambda_1+\lambda_2)}\right]. \quad (26)$$

Since $E_J \propto S$ and $E_Q \propto 1/S$, $E_J/E_Q \ll 1$ is satisfied for the system with small $S$. Therefore, we assume small Josephson junction and set $S = 0.01\ \mu$m$^2$, $\epsilon_r \sim 10$, $a = 1$ nm and assume $a \gg \lambda_{1,2}$. Then, $\tilde{A} \sim 10^{-2}$.

### B. Experimental measurement

From the above estimate, $A \sim 10^{-3}$ for case (I) and $\tilde{A} \sim 10^{-2}$ for case (II), so the asymmetry is rather small in the experimental settings, but we can measure the $2\omega$ response $V_{2\omega}$ to the AC driving current $I_x(t) = I_a \cos\omega t$ with small $\omega$ with a high precision. Assuming $\omega$ is small compared to the characteristic frequency of the dynamics, we can calculate the $2\omega$ component of the response voltage by the adiabatic approximation:

$$V_{2\omega} = \frac{\omega}{2\pi}\int_0^{2\pi/\omega} dt \cos(2\omega t) V(I_a\cos\omega t)$$
$$= \frac{1}{4\pi}\int_0^{2\pi} d\tau \cos\tau \left[V\left(I_a\cos\frac{\tau}{2}\right) + V\left(-I_a\cos\frac{\tau}{2}\right)\right]. \quad (27)$$

Now, we estimate $V_{2\omega}$ for three cases: (A): case (I) with $T = 0$, (B): case (I) with $T > 0$, and (C): case (II). As we discussed, the asymmetry of $V$ is pronounced near the critical value of $i_x$ or $\tilde{i}_x$, so to obtain large $V_{2\omega}$ we set the amplitude of the external voltage $I_a$ near these critical currents, i.e., (A) $I_c$, (B) $i_{c2}I_c$, and (C) $\tilde{i}_{c,bl}^{L/R} e/(RC)$.

For the case (A), i.e., case (I) with $T = 0$, if we set $I_0 > I_C$, the above measurement of $2\omega$ component reflects the difference of $i^R_{c1}$ and $i^L_{c1}$. We set the critical current density $I_c/S = 100$ A/cm$^2$ and the resistance times area $RS = 10^{-5}\ \Omega\,\mathrm{cm}^2$, and the capacitance $C/S \sim 10^{-5}$ F/cm$^2$, where we used Eq. (24) with $a = 1$ nm and $\epsilon_r = 10$. Then we get $r^{-1} \sim 0.1$, and for $A \sim 10^{-3}$, $A' = 0.5A$, the numerical calculation yields $V_{2\omega} \sim 10^{-3} RI_c \sim 1\ \mu$V.

Next, we consider case (B), i.e., case (I) with $T > 0$. We use the same parameters as case (A) and set $T = 50$ K. Then, the numerical calculation yields $V_{2\omega} \sim 10^{-3} RI_c \sim 1\ \mu$V. For case (C), i.e., case (II), for $\tilde{A} = 10^{-2}$ and $\tilde{A}' = 0.5\tilde{A}$, the numerical calculation yields $V_{2\omega} \sim 10^{-2} e/C \sim 1\ \mu$V, where we used the parameters $C/S \sim 10^{-5}$ F/cm$^2$ and $S = 0.01\ \mu$m$^2$. In summary, $V_{2\omega}$ is about 1 $\mu$V for junctions with low carrier density, e.g., FeSe, on one side of the junction, and a conventional superconductor with higher carrier density on the other side of the junction, and it can be measured by the current experimental technology.

### C. Conclusion

We have shown that, in inversion asymmetric Josephson junctions, the nonreciprocal $I_x$-$V$ characteristic is realized if we include the asymmetry of the charging energy both for the system with $E_J/E_Q \gg 1$ and $E_J/E_Q \ll 1$. As we discussed, the nonreciprocity induced by the nonlinear capacitance can be experimentally measured.

## ACKNOWLEDGMENTS

This work was supported by JST CREST Grants No. JPMJCR1874 and No. JPMJCR16F1 and JSPS KAKENHI (Grants No. JP18H03676, No. JP26103006, and No. JP18J21329).

[1] Y. Tokura and N. Nagaosa, Nat. Commun. **9**, 3740 (2018).
[2] S. Kitamura, N. Nagaosa, and T. Morimoto, Commun. Phys. **3**, 63 (2020).
[3] M. V. Berry, Proc. R. Soc. London A **392**, 45 (1984).
[4] T. Morimoto and N. Nagaosa, Sci. Adv. **2**, e1501524 (2016).
[5] D. Jalas, A. Petrov, M. Eich, W. Freude, S. Fan, Z. Yu, R. Baets, M. Popović, A. Melloni, J. D. Joannopoulos, M. Vanwolleghem, C. R. Doerr, and H. Renner, Nat. Photonics **7**, 579 (2013).
[6] F. Fratini, E. Mascarenhas, L. Safari, J.-P. Poizat, D. Valente, A. Auffeves, D. Gerace, and M. F. Santos, Phys. Rev. Lett. **113**, 243601 (2014).
[7] A. Rosario Hamann, C. Muller, M. Jerger, M. Zanner, J. Combes, M. Pletyukhov, M. Weides, T. M. Stace, and A. Fedorov, Phys. Rev. Lett. **121**, 123601 (2018).
[8] G. Carapella and G. Costabile, Phys. Rev. Lett. **87**, 077002 (2001).
[9] J. B. Majer, J. Peguiron, M. Grifoni, M. Tusveld, and J. E. Mooij, Phys. Rev. Lett. **90**, 056802 (2003).
[10] F. Raissi and J. E. Nordman, Appl. Phys. Lett. **65**, 1838 (1994).
[11] P. Recher, Y. V. Nazarov, and L. P. Kouwenhoven, Phys. Rev. Lett. **104**, 156802 (2010).
[12] F. Hassler, Y. V. Nazarov, and L. P. Kouwenhoven, Nanotechnology **21**, 274004 (2010).
[13] J. Hu, C. Wu, and X. Dai, Phys. Rev. Lett. **99**, 067004 (2007).
[14] S. Savel'ev and F. Nori, Nat. Mater. **1**, 179 (2002).
[15] M. J. Martínez-Pérez and F. Giazotto, Appl. Phys. Lett. **102**, 182602 (2013).
[16] A. Kamal, A. Roy, J. Clarke, and M. H. Devoret, Phys. Rev. Lett. **113**, 247003 (2014).
[17] K. K. Likharev, *Dynamics of Josephson Junctions and Circuits* (Gordon and Breach Science Publishers, New York, 1986).
[18] M. Tinkham, *Introduction to Superconductivity* (Courier Corporation, New York, 2004).
[19] A. O. Caldeira and A. J. Leggett, Ann. Phys. **149**, 374 (1983).
[20] K. K. Likharev and A. B. Zorin, J. Low Temp. Phys. **59**, 347 (1985).
[21] M. Jona-Lasinio, O. Morsch, M. Cristiani, N. Malossi, J. H. Müller, E. Courtade, M. Anderlini, and E. Arimondo, Phys. Rev. Lett. **91**, 230406 (2003).
[22] M. Büttiker, H. Thomas, and A. Prêtre, Phys. Lett. A **180**, 364 (1993).
[23] M. Buttiker, J. Phys.: Condens. Matter **5**, 9361 (1993).
[24] T. Christen and M. Buttiker, Phys. Rev. Lett. **77**, 143 (1996).
[25] Z.-s. Ma, J. Wang, and H. Guo, Phys. Rev. B **59**, 7575 (1999).
[26] B. Wang, X. Zhao, J. Wang, and H. Guo, Appl. Phys. Lett. **74**, 2887 (1999).
[27] P. Hanggi and F. Marchesoni, Rev. Mod. Phys. **81**, 387 (2009).
[28] J. L. Garcia-Palacios and F. J. Lazaro, Phys. Rev. B **58**, 14937 (1998).
[29] P. Hänggi, P. Talkner, and M. Borkovec, Rev. Mod. Phys. **62**, 251 (1990).
[30] S. H. Strogatz, *Nonlinear Dynamics and Chaos: With Applications to Physics, Biology, Chemistry, and Engineering* (CRC Press, Boca Raton, 2018).
[31] Y. M. Ivanchenko and L. A. Zil'berman, Zh. Eksp. Teor. Fiz. **55**, 2395 (1968) [Sov. Phys. JETP **28**, 1272 (1969)].
[32] V. Ambegaokar and B. I. Halperin, Phys. Rev. Lett. **22**, 1364 (1969).
[33] J. Guckenheimer and P. J. Holmes, *Nonlinear Oscillations, Dynamical Systems, and Bifurcations of Vector Fields*, Applied Mathematical Sciences (Springer-Verlag, New York, 1983).
[34] H. Risken and T. Frank, *The Fokker-Planck Equation: Methods of Solution and Applications*, 2nd ed., Springer Series in Synergetics (Springer-Verlag, Berlin, Heidelberg, 1996).
[35] L. P. Fischer, P. Pietzonka, and U. Seifert, Phys. Rev. E **97**, 022143 (2018).
[36] A. C. Barato and U. Seifert, Phys. Rev. Lett. **114**, 158101 (2015).
[37] P. Pietzonka, A. C. Barato, and U. Seifert, Phys. Rev. E **93**, 052145 (2016).
[38] H.-M. Chun, L. P. Fischer, and U. Seifert, Phys. Rev. E **99**, 042128 (2019).
[39] G. Schön and A. D. Zaikin, Phys. Rep. **198**, 237 (1990).
[40] A. D. Zaikin and D. S. Golubev, Phys. Lett. A **164**, 337 (1992).
[41] L. S. Kuzmin, Y. A. Pashkin, D. S. Golubev, and A. D. Zaikin, Phys. Rev. B **54**, 10074 (1996).
[42] D. S. Golubev and A. D. Zaikin, Phys. Lett. A **148**, 479 (1990).
[43] A. I. Coldea and M. D. Watson, Annu. Rev. Condens. Matter Phys. **9**, 125 (2018).